Point by Point Gain Calibration of the Dark Matter Time Projection Chamber

by

Albert H. Lee

Submitted to the Department of Physics
at the Massachusetts Institute of Technology
on May 7, 2010, in partial fulfillment of the requirements
for the degree of Bachelor of Science in Physics

Abstract

Since 1975 a growing body of astronomical evidence has given increasing credibility to the existence of dark matter. Once a simple proposition by Fritz Zwicky to explain discrepancies in the virial motion of galaxy clusters, dark matter can now explain galactic rotation curves, the hierarchical structure of the universe, and the gravitational lensing of the bullet cluster. Nonetheless, the exact particulate nature of dark matter remains a mystery. The Dark Matter Time Projection Chamber (DMTPC) is a directional detection experiment that will be able to measure the energy, length, and direction of nuclear recoil tracks induced by incoming weakly interacting massive particles (WIMPs). In this thesis I analyze nonuniformities in the CCD images used to record the nuclear recoils. I then identify the source of the nonuniformities and describe a method for calibrating the CCD images. The method improves the energy resolution by decreasing the uncertainty by a factor of 4 for the bottom time projection chamber (TPC) and a factor of 3 for the top TPC.

Thesis Supervisor: Gabriella Sciolla

Title: Associate Professor of Physics

Acknowledgments

I am fortunate to have had the guidance and assistance of many people in the DMTPC collaboration. First and foremost I must thank Professor Gabriella Sciolla, who supervised me during the two years I have been with the DMTPC group. She introduced me to several interesting projects and always offered great advice. This thesis only amounted to something because of her guidance and support. Similarly, I owe my maturing as a scientist to her spot-on mentoring.

I would also like to thank the graduate students Jeremy Lopez, Shawn Henderson, Asher Kaboth, and Cosmin Deaconu for passing down their wisdom and being patient with my numerous questions about the mysteries of ROOT. I want to thank Professors Peter Fisher and Jocelyn Monroe and Postdoc James Battat for providing great input during group meetings. Often, a nagging problem could be simplified and tackled after consulting with their collective intellect. Fellow undergraduates Tom Caldwell (now pursuing his PhD) and Timur Sahin also receive my thanks. Tom was the mastermind behind the basic analysis framework I modified for this thesis. Timur, in addition to being another great computational resource, helped me operate the detector. Finally, I have endless gratitude for Denis Dujmic, who helped me troubleshoot various developments countless times, and without whom DMTPC would cease to function altogether.

Contents

List of Figures

Chapter 1

Introduction

Around 1934 the Swiss astronomer Fritz Zwicky discovered the first hints of evidence for a mysterious substance called dark matter [1]. His previous interests in supernovae and distant galaxy clusters had led him to study the masses of clusters. After his first rough calculation, he immediately realized there was a discrepancy in the contemporary understanding of astronomy. The virial theorem and the mass to light ratio of stars (measured from a local stellar system), both of which were well-supported concepts, produced estimates for cluster mass that disagreed by a ratio of 500 to 3 [2]. Zwicky posited the existence of a dark matter that would compensate for the lack of stellar mass [3].

Zwicky's claims were ignored for 40 years until Vera Rubin published results in 1975 showing that the orbital speed of stars in spiral galaxies remains constant in the disk region outside the central bulge. Such a velocity distribution is best explained by either a failure in general relativity or the presence of an invisible matter [4].

Within the last couple decades studies in gravitational lensing have shown that most galaxies and clusters warp photon trajectories enough to suggest that the bulk of their mass is not represented by the visible stars. A detailed observation of the Bullet Cluster in 2007 provided strong evidence for particulate dark matter [5]. The Bullet Cluster, as we see it now from the Earth, consists of two galaxies right after a collision. The stars, dust and gas from the two galaxies experience drag as they move past each other due to electromagnetic forces within the ionized gas. On the other

hand, dark matter barely interacts. Correspondingly, a visible light image of the cluster shows stars from the two galaxies clumped in the middle whereas an analysis of gravitational lensing reveals that the majority of the mass (i.e. the dark matter) from either galaxies has moved past the other without clumping in the middle. It is clear how to connect this to particulate dark matter, but difficult to explain using a form of modified gravity.

In section 2.1 I explain the physics behind galactic rotation curves, the virial theorem, and gravitational lensing. Other pieces of evidence pointing to dark matter include the cosmic microwave background (CMB) radiation, the curvature of the universe, and cosmological structure formation. I will focus on cold dark matter and its implications regarding the history of structure formation.

In section 2.2 I describe the structure and function of the Dark Matter Time Projection Chamber (DMTPC) detector. The basic concept of DMTPC is to use CF_4 gas as a target mass that interacts with dark matter particles. During a dark matter particle collision, a nucleus form a CF_4 molecule recoils, ionizing the surrounding gas. The signal from the ionization track is amplified and imaged. The goal of DMTPC is to extract directional information from the images and to determine the velocity distribution, i.e. the direction and speed, of dark matter particles. The ability to directly detect these particles and surmise their direction and energy is crucial for understanding the physics of dark matter as well as the structure of the Milky Way.

Since the DMTPC experiment relies on image analysis of ionization tracks, an accurate image calibration is important for obtaining reliable data. The preliminary data runs exhibited anisotropic features in the images, which would have to be accounted for in some manner. The primary concern of this thesis is to delineate the process of identifying the source of the anisotropies and then developing a method for correcting for those effects. Chapter 3 details the experimental procedures used in the investigation.

In chapter 4 I present the raw data, in the form of charge-coupled device (CCD) image readouts from the detector, as well as the techniques used to analyze the data. Some of these techniques are adapted for use in calibrating the CCD images.

Finally, in chapter 5 I show the results of my analysis. I identify the source of anisotropy principally to be the detector's amplification mesh and field cage. I also introduce a possible method for correcting the anisotropic features and demonstrate that it may improve DMTPC's energy resolution by a factor of 2 to 3.

Chapter 2

Theory and Detector Concept

2.1 On the Existence of Dark Matter

2.1.1 Galactic Rotation Curves

A galactic rotation curve is a graph of the orbital speed of stars as a function of distance from the center of the galaxy. Prior to the first measurements of rotation curves, models of galactic structure implied a very specific shape for rotation curves. The analytical derivation of this shape is relatively straightforward. The early models for spiral galaxies predicted a flat disk structure with a central bulge. This was based on the positions of stars and dust in the sky as well as observations of other galaxies. Indeed, in the absence of light pollution, the bright band of the Milky Way can be seen stretching across the night sky, tracing the plane of the galaxy.

Assuming the the density of mass in the galactic disk is constant, and ignoring the concentration of matter at the center of the galaxy, I can approximate the strength of the gravitational field on a mass m at a distance r from the center. Let dM be a differential component of the total mass M inside the radius r. If the disk is thin enough, all dM within r exert forces on m that are parallel to the galactic plane. Thus, I can ignore the third dimension running perpendicular to the disk. If I stretch the galaxy in the two remaining dimensions by a factor a so that m sits at a radius ar, the distance to every dM element is increased by a, which means the gravitational

pull is decreased by a factor a^2. In order to keep the mass density constant after stretching, I replace dM with $dM' = a^2 dM$. This increases the overall gravitational pull by a factor of a^2, canceling out the decrease in gravity due to increased distance. This is precisely the same calculation required to find the gravitational field at a radius ar in the original unstretched galaxy. Therefore, the total gravitational pull from the disk is constant for all r.

The gravitational pull from the galactic bulge can be approximated using a spherical mass at the center. The field strength then comes out to be proportional to r^{-2}. Of course, this only holds outside the galactic bulge. Based on observations of galaxies and the reasonable assumption that the brightness and density of stars are roughly proportional to the mass density in a galaxy, most of the matter in a spiral galaxy is expected to be located in the central bulge. For circular orbits, the equation for gravitational acceleration is

$$|\ddot{\vec{x}}| = \frac{\dot{\vec{x}}^2}{r} \tag{2.1}$$

$$u \equiv |\dot{\vec{x}}| \quad \propto \quad (fr^{-1} + r)^{1/2}. \tag{2.2}$$

Thus, the theoretical rotation curve for a disk-like spiral galaxy has the form $u \propto (fr^{-1}+r)^{1/2}$ where f is the ratio between the gravitational field strengths of the bulge and the disk. For typical values of f, the rotation curve looks like the dotted line A in figure 2.1.

However, measurements of spiral galaxies show flat rotation curves [7]. Such a phenomenon would require the majority of the visible mass in spiral galaxies to be located in the arms, which directly contradicts observations. Constant orbital velocities at all radii r means that the gravitational force is proportional to r^{-1}. There are infinitely many mass distributions that would lead to such a force-radius relationship but many theories and simulations tend to favor a spherical dark matter distribution. If the gravitational pull from a spherical mass is proportional to r^{-1},

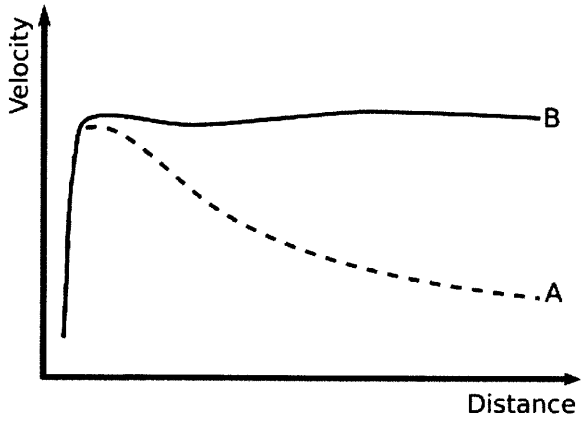

Figure 2.1: Galactic rotation curves show the mean orbital speed of stars as a function of radial distance from the center of a galaxy. This schematic plot compares a rotation curve theoretically derived from the distribution of visible mass in a generic spiral galaxy (A) with a rotation curve measured by observing the same generic galaxy (B). Copied from [6] under GNU Free Documentation License.

the total mass inside the radius r is proportional to r, that is,

$$\int_0^r \rho(r')r'^2 dr' \propto r. \tag{2.3}$$

This approximation gives a dark matter density of $\rho_0 r^{-2}$. The spherical structure is called a dark matter halo, and it is theorized to account for 95% of the matter in our own Milky Way galaxy.

2.1.2 Cold Dark Matter

Given that dark matter does not interact with light, it must be neutral. Also, it cannot interact through the strong force because it would couple too strongly to baryonic matter to match observational data. Dark matter obviously has mass and exerts a gravitational pull, and it may interact through the weak force.

Cosmology offers some extra clues regarding the particulate nature of dark matter. Since dark matter is purported to account for approximately 83% of the matter in

the universe, it plays a significant role in the large-scale structural evolution of the universe. Simulations of structure formation show that hot dark matter (relativistic dark matter) leads to fragmentation. That is, large sheets of matter break down into clumps, giving rise to superclusters and eventually individual galaxies. Cold dark matter (non-relativistic dark matter) results in the opposite effect, a hierarchical history where stars and galaxies form first before eventually coalescing into clusters [8].

Even without running the simulations first hand, one can intuitively grasp the mechanism behind these effects. Hot dark matter particles have a greater average energy and speed than cold dark matter particles. This makes them less susceptible to gravitation, so that they need travel longer along their trajectories to experience a comparable deflection towards aggregations of mass. Regions of higher density form on larger scales and take more time to develop finer structures.

It turns out that the hierarchical structure formation predicted in cold dark matter simulations has an end state closer to the large-scale structure mapped by current sky surveys. One theoretical class of particles that would fit the parameters of cold dark matter would be Weakly Interacting Massive Particles, or WIMPs. The identity of WIMPs is unknown and they require an extension of the Standard Model of particle physics. However, increasingly sensitive detectors are narrowing down the parameter space that is expected to bound the elusive WIMP.

2.2 DMTPC: The Dark Matter Time Projection Chamber

2.2.1 Principles of Directional Detection

There are several promising direct dark matter detection experiments underway. Some experiments, such as CDMS, look for weak interactions with energy distributions that cannot be explained using any known particles [9]. DAMA operates on the principle that the Earth's orbit is expected to introduce an annual modulation in the WIMP counting rate [10]. Nearly all models of the Milky Way's dark matter

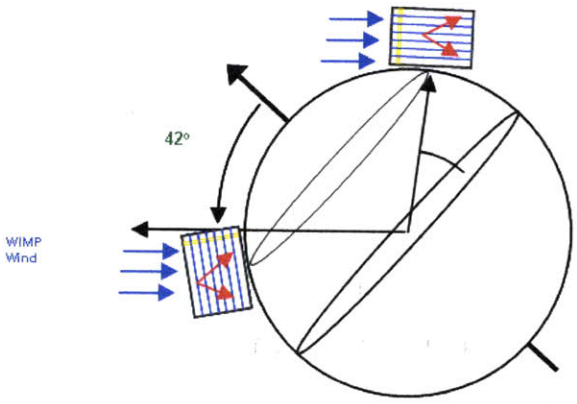

Figure 2.2: This shows how a directional detector can be more sensitive to an anisotropic signal. In the Earth's reference frame a WIMP wind appears to travel in the opposite direction of the Sun's galactic trajectory. A detector positioned at 42 degrees latitude detects particles traveling vertically and horizontally during different times of the day. This daily modulation would be an indicator that the signal comes from a celestial source that moves independently of the baryonic matter in the local Solar neighborhood. Adapted from [12].

halo show that it moves and rotates independently of the visible part of the galaxy. In the simplest model the dark matter halo is a non-relativistic gas in thermodynamic equilibrium, which leads to a Maxwell-Boltzmann velocity distribution with $\sigma = 155$ km/s. There is no overall rotation in this model, so while the Sun orbits around the galactic center, WIMP particles appear to move at the same speed from the opposite direction within the Sun's reference frame. At the current position of the Sun's orbit, this direction is within the constellation Cygnus. The Earth's orbital speed of 30 km/s superposed on the Sun's current velocity of 220 km/s results in the annual modulation of the WIMP signal. However, the effect is a few % and the signal is difficult to distinguish from background sources with annual modulations [11].

The primary motivation for the DMTPC experiment is to use an alternate method that measures the *direction* of WIMPs to increase the signal to noise ratio of direct detection efforts (figure 2.2). The ability to resolve the direction of WIMPs is im-

portant for determining whether an annual modulation comes from actual WIMPs or a seasonal background source. No background is predicted to have directionality correlated to Cygnus [11]. In fact, no background is expected to be correlated with any direction in the sky. Baryonic matter in the vicinity of the Solar neighborhood roughly orbits with the Sun, so any radiation from baryonic sources would be isoptropic. Also, backgrounds from the Earth or the Sun would not be correlated with a celestial direction in the detector's reference frame. Although more complex halo models incorporating rotation and caustics theorize velocity distributions that may not specifically point to Cygnus, there is generally an anisotropy towards some celestial coordinate that can be observed by a directional detector. An additional benefit of the DMTPC experiment is that, with increased resolution, it could become an astronomical tool for mapping the WIMP velocity distribution and probing the structure of the galaxy.

In order to function as a directional detector, when a WIMP collides with a target particle, DMTPC should yield all the measurements necessary for reconstructing the direction and energy of the original WIMP. Since WIMPs are not easily observed in traditional detectors, i.e. they do not themselves leave any ionization tracks, the experiment uses the direction and energy of the recoiling target particle to estimate the velocity of the WIMP. The uncertainty from a single interaction event is relatively large due to the spread in the Maxwell-Boltzmann distribution as well as the recoiling angle of the target nucleus. However, as few as 11 events per year are enough to observe a definite anisotropy [13].

2.2.2 Detector Concept

The detection principle used by each iteration of DMTPC is shown in figure 2.3. It uses CF_4 gas molecules as its target particles. CF_4 is ideal for the experiment because it is non-toxic, non-flammable, has high scintillation efficiency, and a low diffusion rate. When a WIMP collides with a CF_4 molecule, a fluorine nucleus is ejected. Since fluorine nucleus has spin $\frac{1}{2}$, the detector is sensitive to spin-dependent interactions. For the WIMP energy range of interest, the recoiling fluorine nucleus should travel 1-

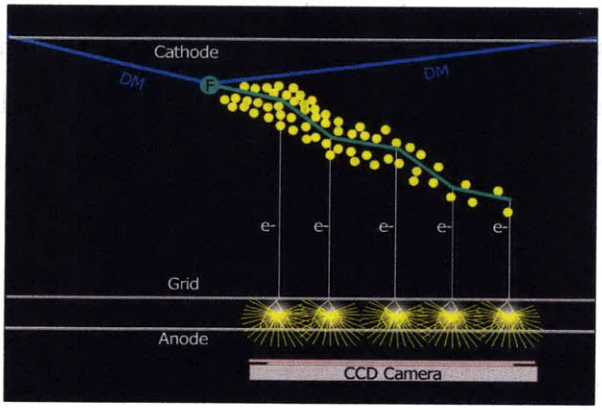

Figure 2.3: A diagram of the detector principle of DMTPC. A dark matter particle collides with a fluorine nucleus through the weak interaction and exits the detector without leaving any other signatures. The recoiling nucleus ionizes the surrounding CF_4 gas, and the resulting electrons drift down to the grid (mesh). There, the high voltage of the amplification region induces an avalanche, producing scintillation photons which are recorded by a CCD camera. Adapted from [12].

2 mm. As the nucleus jostles the surrounding CF_4 it loses energy and ionizes the gas. The number of the freed electrons and their positions are proportional to the total energy of the recoiling nucleus and the corresponding spatial energy distribution.

The gas is contained inside a sealed chamber. The chamber has gas flow controls, a conduit for data readout and external controls, and windows for observing scintillation light (figure 2.4). Within the chamber, a series of conducting rings spaced about 1 cm apart form a cylinder called the field cage. (I will use the term "time projection chamber", or TPC, interchangeably with the term "field cage".) The rings are connected in series with resistors and a potential difference is applied across the cylinder so that a constant electric field is produced inside the field cage. On one end of the cylinder a conducting mesh and an additional anode plate are attached. The electric field between the mesh and the anode plate (a space called the amplification region) is much greater than the field inside the cage. In order to maximize the fiducial volume, two field cages are attached to each side of a anode plate so that the

electric field is symmetric and points away from the anode plate. The double field cage is oriented inside the chamber so that its axis is vertical.

The freed electrons in a fluorine nucleus ionization track drift along the field lines created by the double field cage. That means electrons in the upper cage drift down and electrons in the lower cage drift up. The volume inside the field cage through which the electrons drift is aptly called the "drift region" or the "drifting region." Because of CF_4's low diffusion rate [14], the ionization track retains its shape as it drifts. When the electrons reach the mesh, they are accelerated by the sudden increase in the field strength. These energized electrons ionize additional gas and create an avalanche of free electrons, amplifying the signal. Scintillation photons from the avalanche travel through the chamber windows and into CCD cameras focused on the amplification region [15].

The amplification region is particularly important to this study. Most of the nonuniform gain is expected to come from the mesh or the anode plate due to either geometrical deformations or physical defects that perturb the electric field. The mesh is made of stainless steel while the anode plate is made of copper. Spacers fashioned from fishing line separate the mesh from the anode plate. Since the plastic spacers prevent avalanches, if a track happens to intersect with a spacer some signal is lost in the intersecting region.

2.2.3 The 10 L Prototype

I used the 10 L prototype of DMTPC in my experiment [16]. Since the 10 L shares the same detection principles as other versions, its distinguishing features are its particular structure and geometry (figure 2.4). The double field cage is made out of stainless steel and stands 40 cm tall with a 13 cm radius. It sits on 1-inch-wide plastic feet, which fit into holes in a quarter-inch copper plate at the bottom of the chamber. The stainless steel chamber itself is also cylindrical with a domed top.

Two cameras are fixed to the top and bottom of the chamber. The field of view (FOV) of the bottom camera is 17.5×17.5 cm^2 while that of the bottom camera is 14.5×14.5 cm^2. These values are calculated by counting the number of spacers

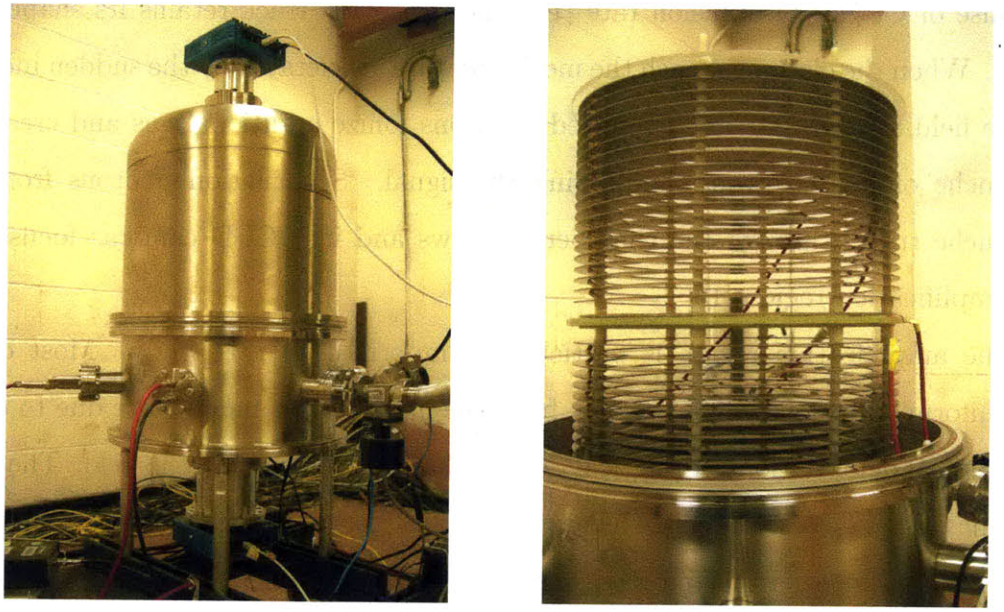

Figure 2.4: The photograph on the left shows the exterior of the chamber. The two CCDs are attached to the top and bottom of the chamber. The wires coming out of the front and left sides of the chamber are used to control the voltage of the field cage. The metal tubing to the right is used to evacuate the chamber and fill it with CF_4 gas. A seal near the middle allows the top half of the chamber to be removed. The picture on the right shows how the field cage is oriented inside the chamber. Each cylindrical TPC is composed of rings connected in series with resistors (visible along the left side of the field cage). Wire leads are connected to the TPCs as well as the meshes and the anode plate. Photo courtesy of Denis Dujmic of the DMTPC collaboration.

across the FOV and multiplying that number by the interval between spacers, 2.5 cm. The fiducial volume then consists of two rectangular prisms totalling approximately 10 L. CCD cameras can be set to trigger on an output signal from a computer. The exposure time can also be controlled from the computer, but the focus must be adjusted manually, which requires detaching the camera from the chamber. A flange around the lens of the camera serves as the point of attachment while also sealing off external light. The detector cannot collect any data while the camera is detached since photons bombard the inside of the chamber.

The computer acquires the following data from the chamber and CCD: the pressure of the gas inside the chamber, the voltage across a field cage, the voltage across the amplification region, the temperature of the CCDs, and the readout from the CCD chips. The readout is saved as a two-dimensional histogram by a ROOT program. Each CCD has 1024×1024 pixels, but during analysis the saved images are re-binned 4×4 so that the resulting two-dimensional ROOT histogram (TH2F) has 256×256 bins.

The goal of my project is to perform a point-to-point gain calibration of DMTPC and to remove anisotropies and anomalous features in the images recorded by the CCD cameras. I carry out my analyses after re-binning the TH2Fs and subtracting a bias frame from the images. There are several possible sources of anisotropy in the images: disproportionate sensitivities in different parts of the CCD, opacities in the window, and uneven field strengths in the amplification region.

Chapter 3

Experimental Setup and Procedures

The general purpose of DMTPC is to measure the direction and energy of recoiling nuclei and thereby extrapolate the direction of incoming WIMPs. As detailed in the previous section, ionization tracks from recoiling nuclei are recorded by CCD cameras. In a given run about 1000 TH2F images are saved to a ROOT file. An analysis program then loops over the images and reconstructs the direction and energy of any identified track. In order to accurately measure the energy of a track, it is crucial to understand how the gain varies across the imaged region. The following describes the procedures I used to study and calibrate DMTPC's anisotropic gain.

3.1 Setup

In order to study anisotropies in the CCD image, which are best observed when multiple tracks cover the majority of the fiducial volume, I had to stimulate the entire fiducial volume uniformly. I used a ^{57}Co source since the 0.12 MeV photons produced during its decay are energetic enough to cause nuclear recoils in CF_4 [17]. The strategy was to stimulate the TPC of interest by "shining" the source through the opposite TPC and the central anode plate. This would place the source at a great enough distance to stimulate the entire fiducial volume evenly (figure 3.1). The source

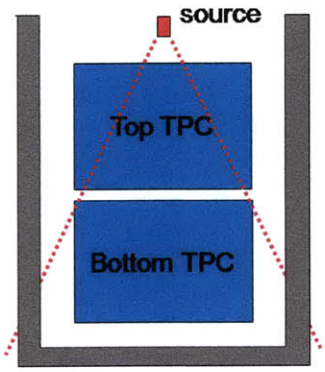

Figure 3.1: In order to study gain nonuniformities the entire fiducial volume must be stimulated evenly. This schematic shows how the bottom TPC would be illuminated. A ^{57}Co source sits above the top TPC pointing into the bottom TPC. As shown in subsection 4.1.2, collimation effects are minimal.

was measured to be 25 mCi on December 19, 2003. ^{57}Co has a 272 day half-life, so during July 2009 its intensity should have been approximately 0.14 mCi or 5×10^6 decays per second. The attenuation coefficient of copper in the 0.12 MeV photon energy regime is about 2.7 cm^{-1} and fluorine nuclei have an interaction cross section of 0.14 cm^2 g^{-1} [18]. The cross sectional area of the fiducial volume is 250 cm^2. At 75 torr I expect about

$$5 \times 10^6 \cdot e^{2.7 \cdot 0.6 \frac{\text{cm}}{\text{cm}}} \cdot \frac{75 \text{ torr}}{760 \text{ torr}} \cdot 0.14 \frac{\text{cm}^2}{\text{g}} \cdot 19 \frac{\text{g}}{\text{mol}} \cdot 5 \text{ L} \cdot (22.4 \frac{\text{L}}{\text{mol}})^{-1} \cdot (250 \text{ cm}^2)^{-1} \simeq 6000 \tag{3.1}$$

interactions (photon induced tracks) per second.

To measure the response of the bottom TPC, I placed the source directly on top of the top TPC's cathode mesh, pointing down, as shown in figure 3.1. To measure the response of the top TPC I placed the source pointing up in an acrylic holding arm that swings under the bottom TPC. The acrylic arm was screwed into the quarter-inch copper plate at the bottom of the chamber. In addition to holding the source, the copper plate ensures that the double field cage remains in the same position from run to run (figure 3.2). I designed and built the arm and plate specifically for this study.

Since the emission rate for the source is very high, during 1-10 sec exposures I

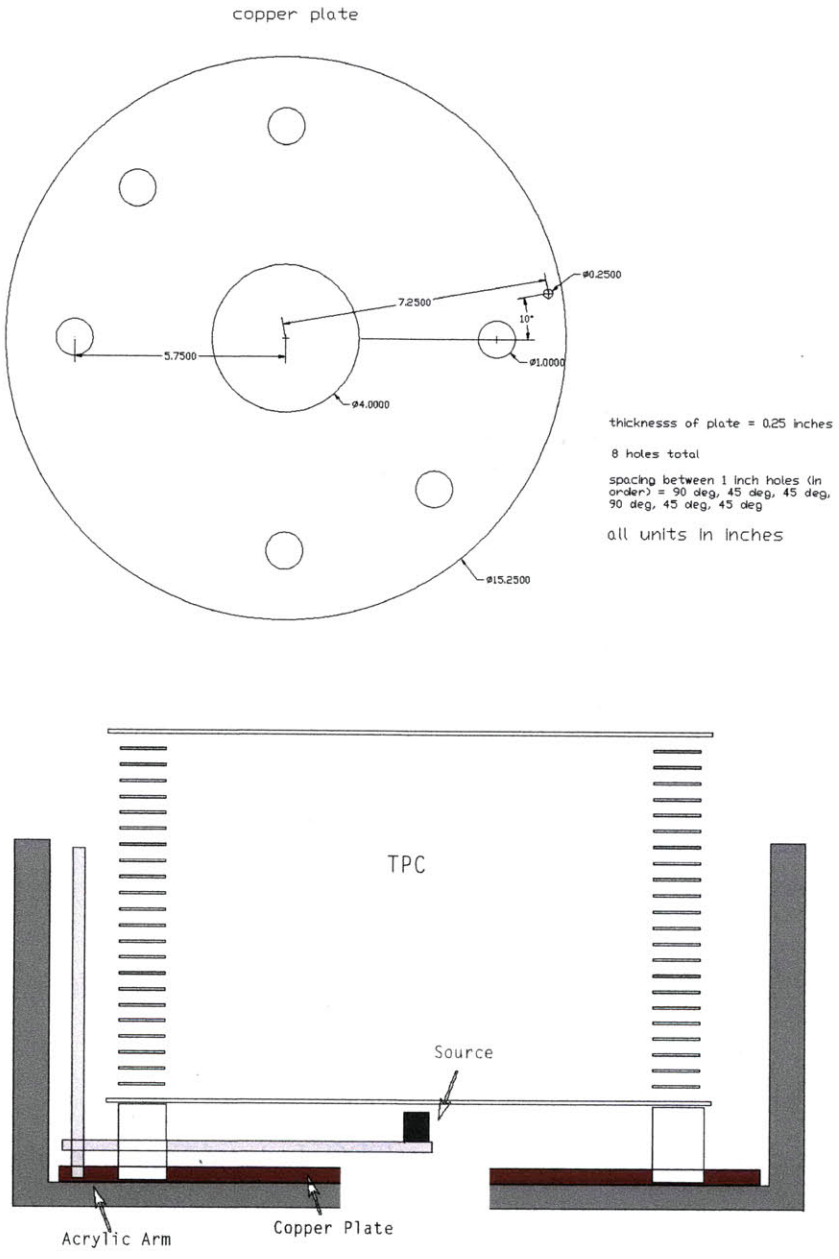

Figure 3.2: These CAD drawings show two components I added to the 10 L prototype specifically for this nonuniformity study: a copper plate for precision positioning of the double field cage and an acrylic arm for holding the source under the bottom TPC. Note how the legs of the field cage sink into the 1-inch holes in the copper plate. The acrylic arm is screwed into the quarter inch hole so that it can swing through the gap in the TPC legs into the space between the bottom TPC and the bottom camera.

could expect the TPC of interest to be evenly populated by photon tracks. The average track has an area of at least 10 bins in the re-binned TH2Fs, which means a pixel is covered by at least one track every second. Then, over a few hours the accumulated data would have negligible noise from Poisson statistics. If the detector had uniform gain, I would expect to see roughly flat images with a 15% drop off near the edges due to the collimation of the source and optical effects. Any deviation from that model would be attributed to some nonuniform detector component such as the amplification mesh or the CCD.

3.2 Procedures

The initial stages of the experiment involved testing various settings to determine the best configuration. The ideal voltage for the field cage was 3 kV while the best voltage for the amplification region was 0.70 kV. Higher voltages tended to induce sparks - sudden discharges from the mesh or the field cage rings. Sparks in turn caused residual bulk images, RBIs, which greatly diminish the number of clean frames that can be used in isotropy studies. Please see Appendix C for more on RBIs.

A typical run included 1000 frames of 5 to 10 second exposures. For certain runs that required low alpha counts, the exposure time was set to 1 second. However, due to readout noise, longer exposure times were more efficient for accumulating large amounts of data. I integrated the frames from each run by adding the sequence of photon counts for each TH2F bin. I also divided the value of each bin by N, the number of frames used in the integration, to ensure that the gain and bin values of the image can be compared to those of single frames. This accumulated TH2F is called the "integrated image," and it usually excludes frames identified as having sparks or alphas. Since frames with sparks have much higher bin values than those without sparks, if more than 55000 pixels are above a threshold of 11.4 keV/mm, the frame is labeled as containing a spark. The algorithm for alphas cuts specifies that the projected range must be greater than 10 mm and less than (0.02 mm/keV)·(energy of track)-(2 mm) [19]. Since frames with alphas and sparks were not included in

the integration, N was usually less than the number of frames originally in the run. Additionally, the errors on the bin values were decreased by a factor of $\sqrt{N}$.

The gain has a tendency to change during long runs because the chemical composition of the target gas changes. I calibrated for this effect by scaling the bin values of each non-spark frame so that the total pixel yield would be constant over one run. I found that it was useful for analysis to remove "hot" and "cold" pixels from the integrated images. Hot and cold pixels are pixels that are abnormally high or low due to excessive or diminished sensitivities of certain pixels on the CCDs. The thresholds for hot and cold pixels were determined by parameters discussed in Appendix B. In some integrated images I applied a normalized two-dimensional smoothing window in order to remove Poisson noise and better identify nonuniform features.

The general strategy for the experiment was to determine first whether there are non-uniformities in the gain. This simply involved generating integrated images from a series of runs and seeing whether the CCDs recorded the expected bin values. If the gain were uniform, the CCDs would be evenly illuminated with a 15% drop off near the edges due to source collimation and optical effects. Since the integrated images differed from the predicted form far beyond the error of each bin, the next step was to identify the source of the non-uniformities. This time I carried out a series of runs while rearranging the structure of the detector. I could move and rotate parts of the detector and look for corresponding translations and rotations of non-uniform features in integrated images. Then, by a process of elimination, I could determine which parts of the detector were responsible which features. Since later steps in these procedures were dependent on the results of earlier runs, I leave the detailed information for chapter 4. For a history of runs please see the table in Appendix D.

Chapter 4

Data Collection and Detector Analyses

The general steps in this study were to look for gain nonuniformities, identify the source of nonuniformities, and finally to develop a method to calibrate the nonuniformities. The first runs (01114 to 01118) confirmed the presence of nonuniformities. The left image in figure 4.3 is a normalized integral of the frames from one of the first runs. At this point there were several candidates that could be contributing to the observed nonuniformity: the CCD, the lens, the TPC, the chamber, or the source itself. Over the next series of runs (01245 to 01252 and 01312 to 01319) I eliminated possible causes of nonuniformity by changing the positions of the detector components independently.

4.1 Identifying the Culprit

4.1.1 The Camera

The two principal components of the cameras used in the DMTPC experiment are the lenses and the CCD. The lenses have adjustable focus but no zoom. Since the cameras are placed at a fixed distance from the amplification region, the focus is fixed and the camera has only one allowed configuration. I can then consider the CCD and lenses

together as a single invariable camera. The camera can be responsible for nonuniformities via the lenses or the CCD. The lenses inherently create nonuniformities due to the geometry of optics, but they may have smudges or other impurities that also affect the passage of light. The geometrical effect leads to a $\cos^3\theta$ radial dependence on θ, the angle relative to the lenses' optical axis. The distance from the primary lens to the imaged plane contributes $\cos^2\theta$ to the formula. The effective aperture for an object off the optical axis contributes another $\cos\theta$. The amplified tracks imaged by the camera can be considered as collections of isotropic point sources, so the intensity of the light from the tracks have no angular dependence.

The CCD inevitably introduces nonuniformities because each pixel responds to photons differently. Usually this problem is fixed by calibrating the CCD and using a bias frame. A bias frame is an integrated image created while the shutter is closed. Since the bias frame records the inherent offset of every pixel, by subtracting the bias frame from subsequent frames (taken with the shutter open) I can extract the relevant information. However, if the gain is different for each pixel there would be nonuniform features even after bias subtraction. I can look for any such effects by rotating the camera between runs and seeing if any features rotate with the camera, i.e., see if any nonuniform features remain stationary in the integrated images.

After I rotated the cameras (runs 01245 to 01248), the data showed that all features remained fixed relative to the chamber (figure 4.1). If a camera was rotated 90 degrees clockwise (viewed in the direction of the camera's perspective) the integrated image and all its features appeared to rotate 90 degrees counterclockwise. This means neither the lens nor CCD can be responsible for any non-radial features. The lens may still be responsible for radial optical effects. Using the formula derived earlier and the dimensions of the detector, the optical effect should be a $1 - \cos^3\theta \simeq 10\%$ decrease in efficiency at the edges of the images. To study this effect I moved the other components of the detector relative to the camera. See the section 4.2 below.

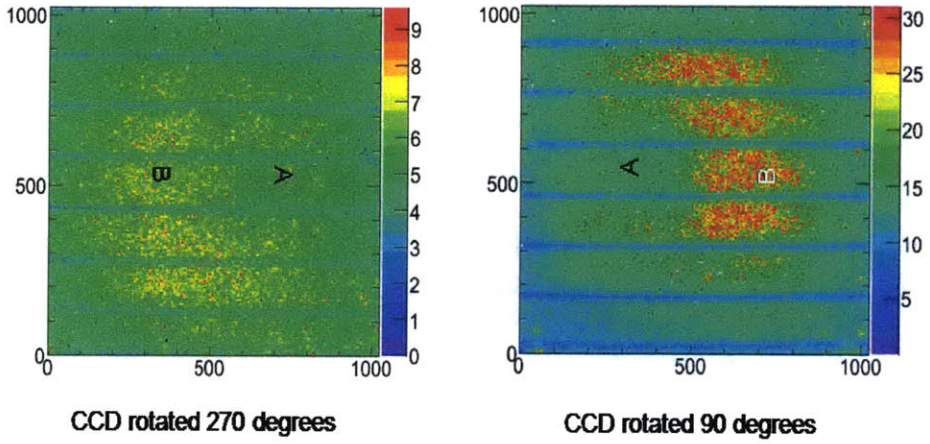

Figure 4.1: These are two examples of integrated images created using frames from two separate runs on DMTPC. The image on the left was created from one of the earliest runs and confirmed the presence of nonuniformities. The horizontal lines are regions of low pixel yield caused by spacers obfuscating scintillation light. The low and high yield patches, respectively marked by the letters A and B, are caused by gain nonuniformities. The image on the right was created with an identical detector configuration, except that the camera was rotated 180 degrees. Since the features A and B do not rotate with the camera, i.e. they do not remain fixed within the frame of the image, we know they are not an effect associated with the lens or CCD.

4.1.2 The Source

The collimation of the ^{57}Co source largely determines the integrated image I expect to see from a detector with uniform gain. If the beam profile is narrow, it is difficult to measure nonuniform gain where the beam tapers off. In order to ensure the source has a wide enough profile to evenly excite the fiducial volume, I moved the source between runs to look for changes in the integrated image (runs 01326 to 01335). Integrated images are sensitive to the counting rate as well as the gain. If the source is constant in time I can measure the gain nonuniformities. If I move the source the integrated images effectively become measurements of variability in the beam intensity. Although it was unlikely, moving the source would also confirm that the nonuniformities were not due to some flaw in the source itself.

I used a 9 bin by 9 bin patch in a corner of the integrated images to measure the intensity. I placed the source directly in line with the part of the amplification region

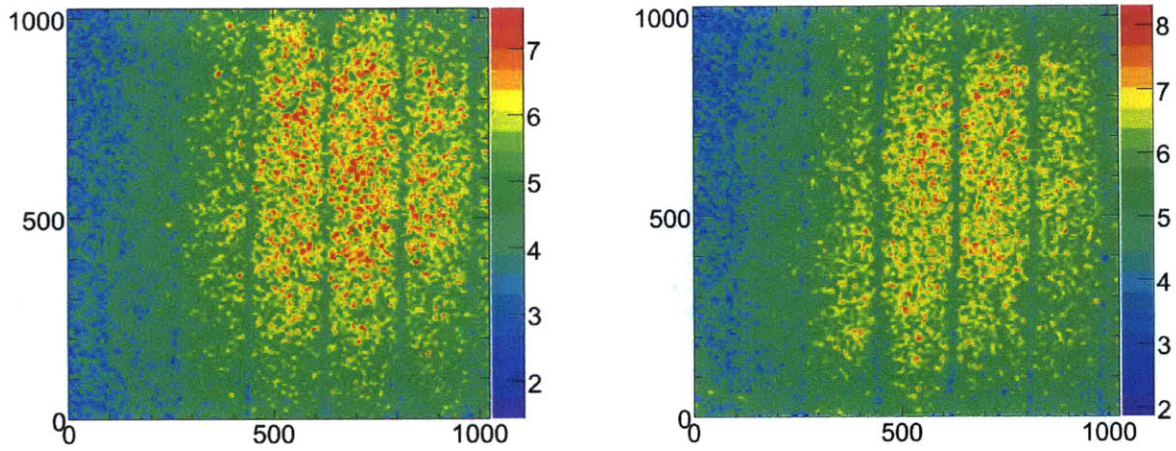

Figure 4.2: In these two integrated images, the source was moved. In the left image the source is in the upper right corner of the image and in the right image it is in the bottom left corner. The nonuniform features stay fixed while the relative gain is slightly increased in the corner with the source (pay particular attention to the low gain region along the left edge). If I take the local average of a 9 by 9 bin area it turns out the position of the source results in a difference in the gain less than 15% of the maximum difference in gain across a single image.

imaged by the corresponding patch of pixels in the CCD. Then I averaged the bin values in the patch for the resulting integrated image. I repeated these steps with the source in the center of the detector and then in the opposite corner. The total change in the average intensity was less than 15% of the greatest difference in the gain for a single integrated image (figure 4.2).

4.1.3 The TPC

The TPC can be expected to introduce nonuniformities due to unequal gain at the amplification region. If irregularities in the mesh or the anode plate cause the width of the amplification region or the conductivity of the material to vary over imaged the plane, the gain would be uneven. Although the voltage that accelerates incoming ions should be constant across the amplification region, scintillating avalanches may be nonlinear at the length scale of the region's width. The drift region is less likely to introduce nonuniformities because the ionization efficiency and the probability of recombination are constant in the region.

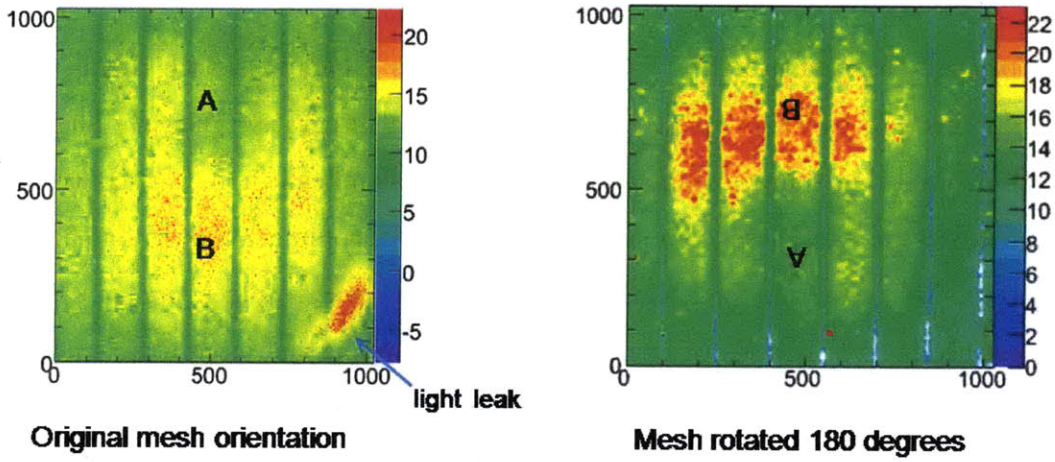

Figure 4.3: In these two images, only the TPC was rotated 180 degrees. Features A and B clearly rotate with the TPC, which implies that the TPC is the primary contributor to nonuniformities. The patch in the bottom-right corner of the left image is not a region of high gain, but rather a light leak caused by a loose screw in the camera mount. The left image is shown here to demonstrate the TPC effect, but was excluded from analyses in this study.

Although the detector chamber includes a copper plate that can fix the location and orientation of the TPC, I was able to translate and rotate the TPC by placing the plastic feet outside the holes in the copper plate. I always checked that the field cage was at least 1 inch away from the chamber walls to prevent discharges. The first run after rotating the TPC (run 01313) immediately revealed that the TPC was principally responsible for the nonuniform features (figure 4.3). If I moved or rotated the TPC between runs while keeping the other detector components fixed, the integrated images showed identical movements and rotations of the nonuniform features. Although run 01313 did not identify whether it is the amplification region or drift region that generates such features, it did eliminate the chamber, camera, and source from being the main contributors. I dedicated the rest of the runs (01320-01386) to measuring the shape of the features caused by the TPC.

4.2 Mapping the TPC

In order to measure the TPC nonuniformities I had to isolate them. One way to do this was to remove non-TPC features from integrated images. The earlier runs indicated that source collimation was the only significant non-TPC contributor to the features (nevertheless, compared to TPC effects, collimation is still a small contributor). My technique for isolating the TPC effect was to place the source at different locations over a series of runs and then to combine the integrated images from the runs. There are several ways to combine the images and preserve the TPC features while reducing the collimation effects. The TH2Fs created by combining integrated images are called point to point gain maps. Within a measure of error called the reconstruction uncertainty, these TH2Fs represent the varying gain of the TPC.

4.2.1 Reconstruction Uncertainty

The reconstruction uncertainty is the upper bound uncertainty that a point to point gain map (PPGM) represents the gain nonuniformities caused by the TPC. The reconstruction uncertainty is also the sum of all systematic and statistical uncertainties in a PPGM with the exception of any TPC effects. It can thus be considered the uncertainty that a PPGM will correctly calibrate energies if I only compensate for TPC effects. The motivation for associating the uncertainty of a PPGM with that of the corresponding TPC nonuniformities is that the procedures for creating a PPGM only guarantees that TPC effects (and possibly lens effects) will be correctly calibrated. In previous sections I showed that the other notable sources of nonuniformity, i.e. the lens and the source, only amount to 10 to 15 % effects, so calibrating primarily for TPC effects is a good baseline for creating a PPGM. I can then use the reconstruction uncertainty as an upper bound on the error in energy reconstruction given that a PPGM is used to represent the actual gain nonuniformities.

To calculate the reconstruction uncertainty I used two integrated images, A and B, where the only difference was that B was created using a run where the TPC was shifted in one direction by a distance equivalent to 21 bins or 1.2 cm in the integrated

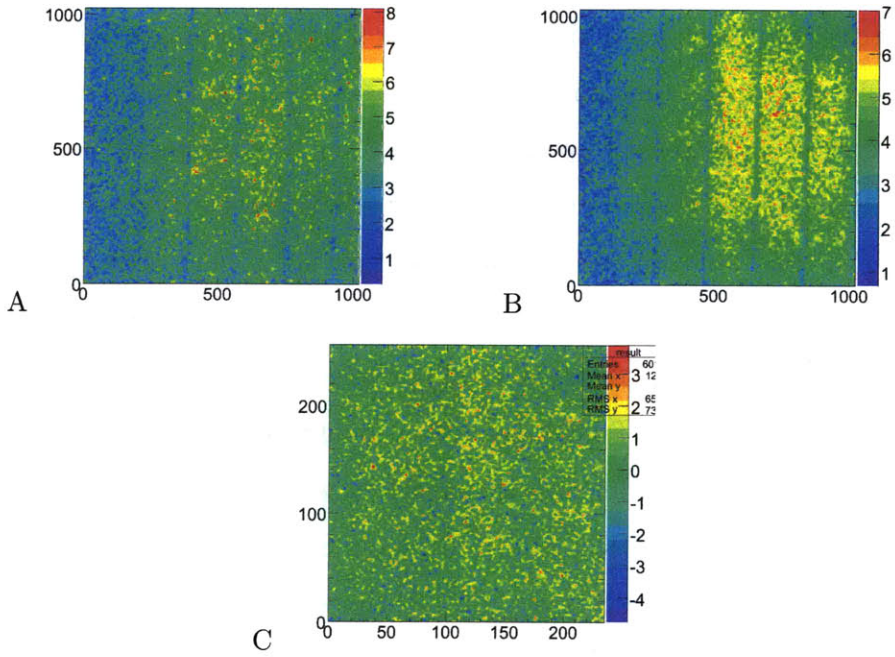

Figure 4.4: These images demonstrate the method for calculating reconstruction uncertainty. The top left image was produced while the TPC was shifted left by about 10 bins in the FOV. The top right image was produced with the TPC shifted to the right by 11 bins. Altogether the 21 bins are equivalent to a shift of 1.2 cm. Both images are smoothed with a 9×9 bin window to ensure that the statistical uncertainties in this calculation are identical to those in PPGMs, which also use 9 bin smoothing windows. The image on the bottom shows the difference between the two images after they have been shifted so that points on the TPC match each other. In effect, I remove TPC-related structures from the bottom image. The RMS of bin values in the bottom image is 0.7 counts while the RMS of the top images is 1.5. An alternate method of using the dimensionless normalized RMS (see text) shows an improvement from 0.4 to 0.1. This suggests that if a PPGM accurately compensates for TPC effects, 75 % of nonuniformities can be eliminated.

image. In figure 4.4, A and B are the top two TH2Fs. I then shifted the bins in image B by 21 bins so that the features from the TPC would line up with those in image A. Of course, this means I had to fill parts of image B with zeroes, so I only analyzed the parts of the TPC imaged in both A and B. Subtracting B from A after the shift, I removed all TPC effects and was left with only residuals in the final image C. If other components of the detector contributed significant nonuniformities they would be visible in C, but C was predominately noise. See bottom TH2F in figure 4.4. Note that image C has a smaller field of view. I used the RMS of image C as

the reconstruction uncertainty. Since I use a 9×9 bin smoothing window to produce point to point gain maps I did the same for images A and B. This would reduce the statistical errors for the point to point gain maps and the reconstruction uncertainty by the same amount. The smoothing window of 9 bins also encompasses the expected sizes of WIMP and neutron tracks, the important signal and noise sources in this experiment.

The RMS of C was 1.0 counts. A total of three independent measurements gave an uncertainty on the RMS of 0.3 counts. The counts can be considered an arbitrary unit because it is only useful for direct comparison with images A and B, which were created using runs with identical exposure times. Since image C was created using two integrated images, its RMS is actually $\sqrt{2}$ times the uncertainty associated with one integrated image. Therefore, the reconstruction uncertainty was 0.7 ± 0.2 counts. To interpret this number I must compare it with an integrated image created with the same exposure times. The RMS of images A and B are both 1.5 counts. Already the RMS values suggest a twofold improvement on the energy resolution if I can remove the TPC effects.

However, a more pertinent comparison is to relate the normalized RMS of the images. That is, before calculating the RMS of an image, I normalize the bin values so that the mean bin value of each image is set equal to some constant. For simplicity I normalize everything to 1 in these studies. Normalization makes the measurement sensitive to the ratio between the RMS and the mean bin value. The higher the ratio, the greater the nonuniformity. This ratio is important for cases where two images may have the same RMS but different mean values. In such a situation, the image with the higher mean value would have smaller nonuniformity-related effects since the ratio between the high and low gain regions would be closer to 1. In dimensionless units, the normalized RMS (NRMS) of images A and B are both 0.4. In image C I subtracted away the mean bin value so I cannot directly compare its normalized RMS to that of A and B. However, if I double the mean value and add it to image C i can relate the NRMSs. This gives me the result 0.1. Thus, with the correct analysis, I find a factor of 4 improvement in energy resolution after applying a PPGM. The

radial lens effect mentioned in subsection 4.1.1 is incorporated into the reconstruction uncertainty and the NRMS.

4.2.2 Secondary Effects

Secondary effects are features in an image that do not represent the gain but are rather caused by an unrelated process during the recording of the image. Point to point gain maps (PPGMs) are combinations of integrated images used to represent the nonuniform gain of the detector. Secondary effects must be removed from integrated images in order to produce an accurate point to point gain map.

One such effect was that some of the frames used to create certain integrated images were found to have alpha tracks. Although the analysis software vetoed all sparks, it missed roughly 5 to 10% of weak alphas because alpha tracks are harder to identify when they occur on top of a patch of photon tracks. However, I found that the offsets caused by alpha tracks are within a standard deviation, so I continued to use the analysis software when generating point to point gain maps.

The other notable secondary effect was a boost in bin values due to the collimation of the source. A point to point gain map relies on the principle that regions of higher gain will result in higher bin values if the source is uniform. Yet, if the beam intensity is higher is some areas, the same phenomenon occurs. As discussed in the following section, the technique used to create point to point gain maps must compensate for or remove this collimation effect.

4.2.3 Point to Point Gain Maps

The primary goal in creating a point to point gain map is to accurately represent the nonuniform gain across the fiducial volume of DMTPC while excluding secondary features that arise from the process of creating the point to point gain map. This mainly involves compensating for effects due to the collimation of the source, since other secondary features are negligible. One method for removing the collimation effect is to move the source evenly over the fiducial volume and to combine the

resulting integrated images in a way that minimizes any effect from the source's beam profile. I placed the source in the north, south, east, and west corners of the detector for four different runs. I considered two strategies for dealing with the collimation effect:

> Strategy 1: Add together integrated images from all four runs assuming that the combined collimation effects would even out. This method would be ideal when the source has a nearly flat beam profile.
>
> Strategy 2: Use a model where the fiducial volume is stimulated evenly outside of the source's beam path due to reflections, back scattering, and secondary collisions. In this case, by removing from each integrated image the high bin values corresponding to the center of the beam, I could produce an accurate point to point gain map. One way to remove these bin values is to compare the integrated images and for every bin select the lowest of the four values. This latter method is better when the collimation is narrow.

I used the first method for the top TPC (figure 4.6) and the latter method for the bottom TPC (figure 4.5). The source was placed below the bottom TPC on the bottom of the chamber while I produced the PPGMs, so the collimation effect was more pronounced for the bottom TPC (figure 4.7). Due to time constraints I did not have data for the bottom TPC while the source was in the preferred location above the top TPC. Since the PPGMs use integrated images they inherently have 9 by 9 bin smoothing. Note that radial lens effects and spacer effects (as well as statistical noise) remain in the point to point gain maps. In fact, only the collimation effect from the source is removed. All other nonuniform components are necessary for PPGMs since they are also present during data runs. If a PPGM is to be applicable to data runs it must be produced with the fewest possible changes to the interior structure of the detector.

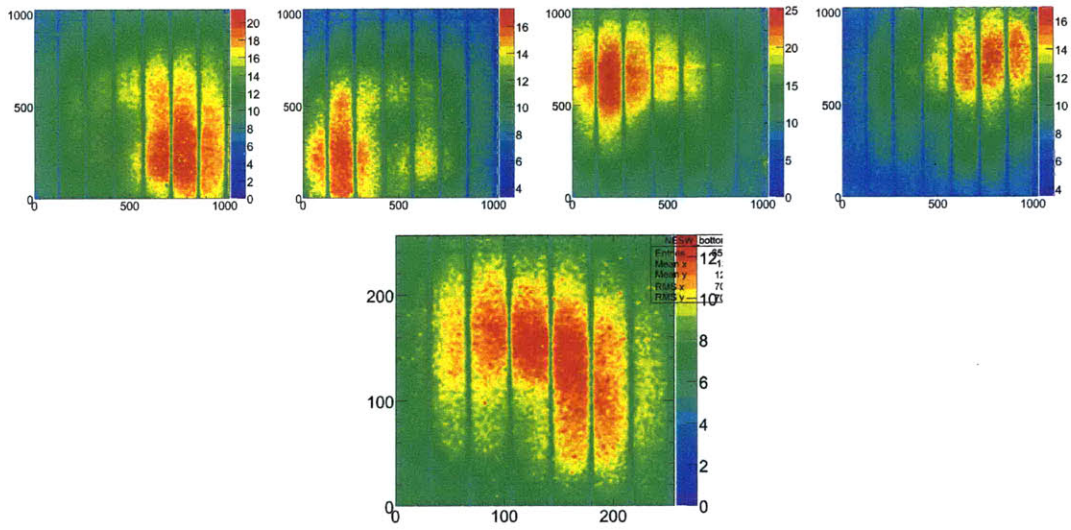

Figure 4.5: This figure shows how a point to point gain map for the bottom TPC can be created from multiple integrated images. The first four integrated images in the top row were produced by placing the source in four different positions. The source positions, from left to right, are north, west, south, and east. North points roughly towards the bottom right in each image. One can clearly see that high intensity regions are correlated with source positions. The bottom image shows the resulting point to point gain map after applying strategy 2.

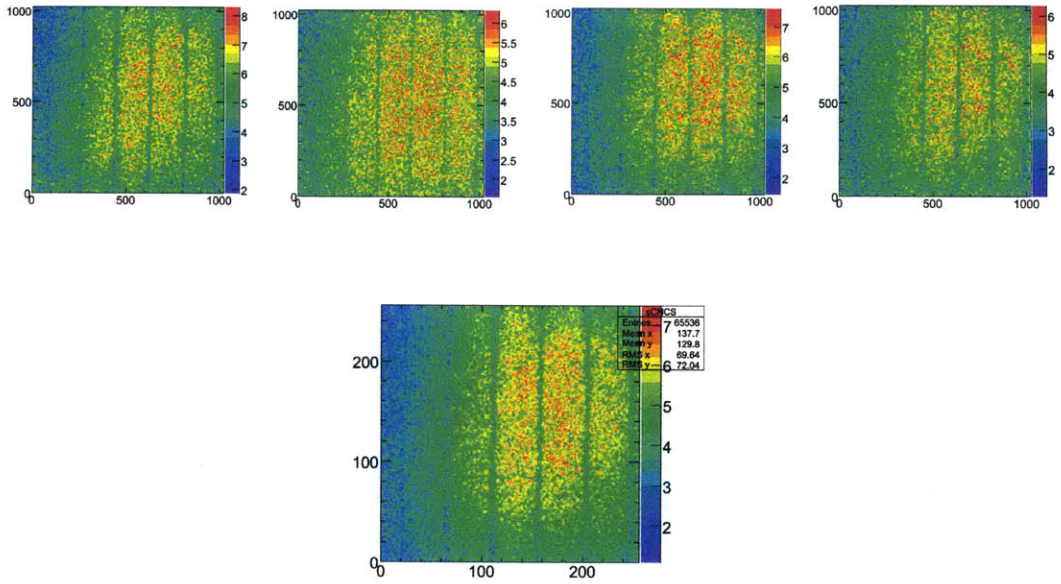

Figure 4.6: This figure shows how a point to point gain map for the top TPC can be created from multiple integrated images. The top four images, from left to right, were taken with the source in the north, west, south, and east corners. North points roughly to the bottom left in these images. The bottom image shows the resulting point to point gain map for the top TPC after applying strategy 1. Note how the collimation effect is less noticeable for the top TPC since the source was farther away.

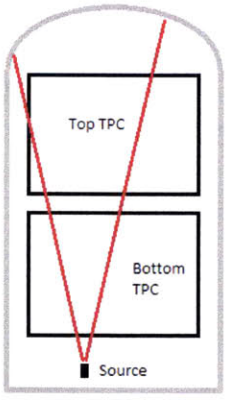

Figure 4.7: A diagram showing why the collimation effect was greater for the bottom TPC. Strategy 1 was used for the top TPC while strategy 2 was used for the bottom TPC.

Chapter 5

Results and Conclusions

5.1 The Gain Correction Map

Point to point gain maps show how the gain of the DMTPC detector varies across the imaged region. In order to calibrate data using this information, I invert the value of each bin. This inverted TH2F is called the gain calibration map. By multiplying each frame in a data run by the gain calibration map I effectively factor out the component of the gain caused by nonuniformities in the detector. I normalize the bin values in each gain calibration map (GCM) to the average bin value. This guarantees that the average reconstructed energy before applying the GCM will be the same as the average energy after applying the GCM. See figure 5.1 for the gain calibration maps of the top and bottom TPCs in the 10 L detector.

As noted in subsection 4.2.1, the standard deviation on reconstructed energies decreases from 1.5 counts to 0.7 counts after calibration with a GCM. Yet, in this experiment, the ratio of bin values between high and low gain regions is the main measure of nonuniformity. So the standard deviation alone is not the best indicator of the accuracy of a calibration method. By comparing the standard deviation to the mean bin value, I can measure the degree of nonuniformity. The normalized RMS (NRMS), a dimensionless number obtained by dividing the standard deviation by the mean value, is one such method for quantifying the calibration accuracy for a given set of frames. As I showed in subsection 4.2.1, the pre-calibrated image in figure 4.4

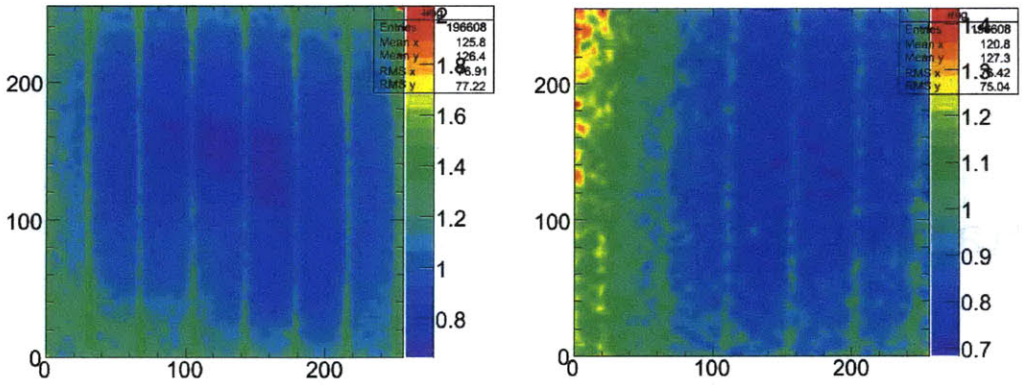

Figure 5.1: The image on the left is the gain correction map for the bottom TPC and the image on the right is the GCM for the top TPC. The average bin values of both GCMs are 1. This ensures that the bin values in calibrated frames are normalized. Note that a smoothing window has been applied, and that spacer and optical effects are incorporated into the GCMs.

has a NRMS of 0.4. Repeating this measurement for both TPCs over the entire set of runs, I find that after applying a GCM the NRMS improved from 0.4 to 0.1 for the bottom TPC and from 0.3 to 0.1 for the top TPC.

5.2 The Physical Consequence

Such an improvement on the energy resolution is crucial for DMTPC. The three most important pieces of information that can be extracted from an image of a track are its visible energy, length, and direction, with energy being by far the most powerful of these measurements. Although direction is a largely independent measurement, energy and length are strongly correlated (figure 5.2). The correlation can be used to determine the type of particle that caused the track, and to discriminate between nuclear recoils and backgrounds such as alphas and electrons. This means that in order to identify whether or not a track is a WIMP signal, and to furthermore measure the energy and direction of a track accurately, it is necessary to maximize the energy resolution. By calibrating with GCMs, DMTPC will be more sensitive to its key variable, directionality.

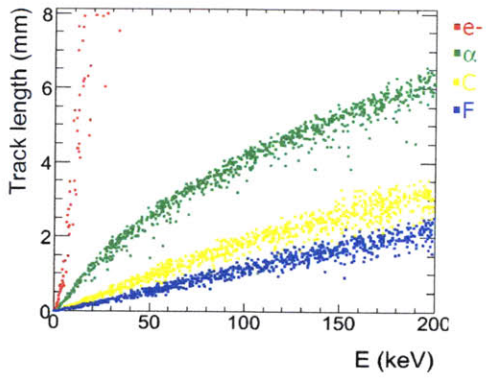

Figure 5.2: This graph shows a strong correlation between energy and track length. The C and F stand for carbon and fluorine nuclei. This information can be used to discriminate between signal and background events. Adapted from [20].

5.3 Conclusion

This study proves that GCMs should be used to calibrate all future DMTPC runs. A GCM only has to be generated once for a series of runs that uses the same detector configuration, so ample time should be allotted to collect enough data for the GCM. Longer integration times should require smaller smoothing windows and lead to more accurate spacer correction. A uniform illuminating source would also circumvent the need to move the source during GCM production. Refining the GCM will be one of the important factors in developing DMTPC for advanced applications, such as WIMP astronomy, which require high accuracy and precision in measuring the energy and direction of recoil tracks.

Appendix A

Glossary

Amplification region: the region of the TPC between the mesh and the anode plate; the high voltage in this region accelerates electrons to induce a scintillating avalanche of ions.

Bias frame: an image (or the average of a collection of images) recorded while the shutter on the camera is closed; used to subtract inherent CCD pixel biases from data.

Drift region: also "drifting region"; the cylindrical volume inside the rings of the field cage through which electrons drift to the amplification region.

FOV: field of view.

Gain calibration map (GCM): the TH2F used to correct frames from runs with a specific detector configuration, via bin by bin multiplication; bin values are inversely proportional to those of the corresponding point to point gain map; bin values are also normalized so that the average bin value is 1.

Integrated image: a TH2F created by adding images from a run (photon counts are added bin by bin); usually excludes frames identified as containing sparks or alphas.

Normalized RMS (NRMS): a dimensionless measure of nonuniformity obtained

by dividing the root mean square of the bin values of an image by the mean bin value; usually measured after smoothing; shows how much the gain across the FOV is offset from the average gain.

Point to point gain map (PPGM): TH2F produced by adding integrated images for different source positions; the point to point gain map is inverted and normalized to be used as a gain calibration map.

Reconstruction uncertainty: the sum of all systematic and statistical uncertainties associated with the detector, excluding TPC effects; the uncertainty of a point to point gain map.

Run: a collection of consecutive frames saved as a single file by root.

Secondary effect: a feature in an image that does not represent the relative gain of the corresponding detector region, but is rather caused by an unrelated process during the recording of the data.

Spark: sudden discharges from the mesh or the field cage rings.

TH2F: the standard image format used in this study; a two-dimensional-histogram object class in ROOT that stores floats as bin values.

Total pixel yield: the sum of all bin values in a single frame.

TPC: time projection chamber; in this thesis, used interchangeably with "field cage".

Appendix B

Appendix: Code for Producing and Using Gain Maps

This appendix provides a guide for using the software developed for PPGM and GCM production. Some familiarity with ROOT is recommended. At the time of this writing, the software is only available to those with access to the DMTPC server.

B.0.1 Producing the Map

The code for producing a gain map can be found in AnalysisFramework/v2/ImageTest.C

When you have runs saved to ROOT files, enter the following commands in CINT:

```
.L ImageTest.C;
ccdN = 0;
TH2F* result = sum("00000",1,1000);
```

"00000" is normally the desired run number and 1000 is normally the total number of frames in run "00000". ccdN is the CCD number (switching between values 0 and 1 will switch between top and bottom CCDs). It is important to note that the top CCD will not always be accessed by the value 0. The value depends on the order in which the CCDs are initialized because they are connected to the server by USB and therefore cannot be addressed by a specific port.

Now "result" points to a TH2F with the integrated image. A canvas should show the integrate image in the top left pad, a history of the total pixel yield in the top right, the locations of probable worm events in the bottom left, and the pixels identified as sparks and corrected for in the bottom right. "result" should not have defects. In the case "result" does show defects, you can adjust the parameters cLim (threshold for cold pixels), hLim (threshold for hot pixels), and sLim (threshold for pixels identified as spark pixels). The parameters should all be loaded into CINT with default values (-1.5, 2.5, and 1.5, respectively). A value of 0 corresponds to a threshold at the image's mean value. A value of 1 corresponds to a threshold at 1σ above the mean value. By default the smoothing window has a size of 9 by 9 pixels.

Repeat these steps with the source in different positions (preferably at least four positions). If the source is outside the detector pointing in, you need exposures at least 5 sec long and take at least 3000 frames per position. For each position, save "result" into a TFile under separate names. At this point there are two options, as explained in subsection 4.2.3. To add all the images, as in Strategy 1, use the commands

```
TH2F* Map;
Map->Add(result1,result2);
Map->Add(Map,result3);
Map->Add(Map,result4);
⋮
```

repeating as necessary. To use Strategy 2 enter the commands

```
.L ImageTest.C;
TH2F* Map;
Map = extract(result1,result2);
Map = extract(Map,result3);
Map = extract(Map,result4);
⋮
```

Finally, invert "Map" with

Map = Invert(Map);

B.0.2 Applying the Map

To modify AnalysisFramework so that gain correction is carried out during analysis, you could add the line

tempimg = tempimg -> Multiply(tempimg,gainimg,1,1);

immediately after the line

tempimg = (TH2F*)d.event() -> ccdData(u) -> Clone("backimg");

in cleanSkim.C, where gainimg is the gain correction map. Keep in mind that drifting pedestals will cause this calibration to be slightly off.

If the FOV of a run is offset from the FOV of the correction map use

Map = Offset(Map,dx,dy);

on the correction map "Map" before running the analysis. dx and dy are the number of bins by which the histogram should be displaced to match the run. You will have to cut any frames with tracks that make it into the non-overlapping region. If the FOV is rotated by a multiple of 90 degrees you have the option of using

Map = rotate(Map,dx,dy);

as needed. These changes should not be necessary if the map is produced with the correct method - i.e. the detector configuration is not modified during or after the calibration runs.

Appendix C

Residual Bulk Images

This appendix discusses some of the characteristics of residual bulk images and lists methods for preventing their occurrence.

Residual bulk images are generally associated with sparks. If a spark is small, the only effect is that the corresponding frame is flooded with light and thus unusable. A function in the analysis software vetoes such frames so that an integrated image is generated only from sparkless frames. However, sufficiently bright sparks will saturate the CCD, and spots as wide as 20 unbinned pixels will persist where the spark occurred in the FOV for up to hundreds of frames (figure C.1). These spots are called residual bulk images (RBI). See [21] and [22] for details.

A single pixel of a CCD consists of a surface silicon dioxide layer (the exposed frontside), an epitaxial layer, and the substrate on which the epitaxial layer is grown. RBIs form when the incident light has a long enough wavelength to penetrate the pixel to the interface between the epitaxial layer and the substrate. For the Alta U6 CCDs used in the 10 L prototype, the threshold wavelength is 7600 Å. If the light is intense enough, freed electrons will gather at the interface and slowly bleed into the readout over subsequent frames. The rate at which the trapped electrons are released from the interface is lower for lower temperatures.

RBIs can be avoided without changing the way DMTPC uses the CCDs. Running at 0.7 kV usually eliminates all sparks. Also, the analysis software corrects for RBIs by replacing pixels identified as RBIs with bin values from before the corresponding

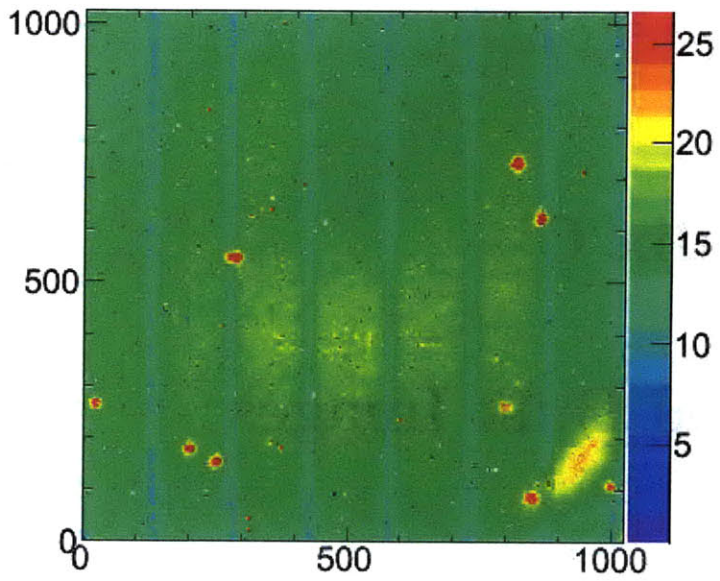

Figure C.1: This image shows an integrated image with several RBIs (red spots). The faint red patch in the bottom right is not an RBI but rather light leaking in from an unfastened camera.

sparks occurred. In case that these methods do not work, there are a few ways to deal with RBIs. Special CCDs such as back-illuminated CCDs or those without epitaxial layers don't encounter this problem. If the current CCD model is used, DMTPC can be designed to illuminate the entire CCD with 7600 Å light before every run and to keep the CCD at low temperatures. This will ensure that every pixel exhibits the same RBI effect for the entire run. Sparks will not leave observable effects since the pixels' epitaxy-substrate interfaces will already be saturated.

Appendix D

List of Runs

Run Numbers	Dates	Comments
00622 - 00626	2009.2.9 - 2009.2.12	Denis Dujmic's preliminary studies
01114	2009.6.23	Testing detector controls
01115 - 01118	2009.6.24 - 2009.6.25	**Bottom TPC study**; voltage to top TPC disconnected
01245 - 01248	2009.7.17 - 2009.7.18	CCD rotated, **not a source of non-radial nonuniformity**; TPC fixed at 180° with respect to June run, **TPC is source of non-radial nonuniformity**
01249 - 01252	2009.7.18	CCD rotated; tried 3 sec exposures
01312	2009.7.28	Source outside, not enough statistics to be useful
01313 - 01317	2009.7.29	TPC moved, **TPC main source of radial nonuniformity**
01318 - 01319	2009.7.29 - 2009.7.30	TPC rotated 45°, additional proof of TPC effect
01320 - 01325	2009.7.31	**Began top TPC study**; tested short exposures
01326 - 01330	2009.8.1	Source moved, looked for collimation effects
01331 - 01335	2009.8.2	TPC moved relative to previous set of runs, tried to isolate TPC and collimation effects
01336 - 01346	2009.8.2 - 2009.8.6	**Measured illumination from outside chamber**; **Lens detached during these runs**, top TPC data unreliable
01347 - 01359	2009.8.6 - 2009.8.7	Attempted detailed study of collimation, couldn't use data because of detached lens; **noticed problems with focus and CCD access #**
01360 - 01363	2009.8.8	Diagnosed problems by turning off CCDs; **Reglued lens to adaptor ring**
01364	2009.8.8	Confirmed both CCDs working
01365 - 01376	2009.8.8 - 2009.8.10	Detailed collimation study; **Select runs used to produce point to point gain maps**
01377 - 01381	2009.8.10	TPC moved to various positions, confirmed TPC effect for top TPC, compared runs to characterize lens effect
01382 - 01386	2009.8.10 - 2009.8.11	High statistics study with short exposure, signal wiped out by readout noise

Table D.1: This table is intended to be a conceptual summary of all runs used in this study. In the "Comments" column independent objectives, settings, or observations are separated by semicolons. Those that are related are separated by commas.

Bibliography

[1] G. Bertone, D. Hooper, J. Silk, arXiv:hep-ph/0404175v2, 21 Apr 2004.

[2] F. Zwicky, "On the Masses of Nebulae and of Clusters of Nebulae", Astrophysical Journal 86:217 doi:10.1086/143864, 1937.

[3] S.M. Maurer, "Idea Man", Beamline (SLAC) 31 (1), 2001.

[4] V. Rubin and W. K. Ford, "Rotation of the Andromeda Nebula from a Spectroscopic Survey of Emission Regions", Astrophysical Journal 159:379 doi:10.1086/150317, 1970.

[5] R. Massey *et al.*, "Dark matter maps reveal cosmic scaffolding", Nature 445 (7125):286290, 18 January 2007.

[6] http://upload.wikimedia.org/wikipedia/commons/5/53/GalacticRotation2.png

[7] V. Rubin, N. Thonnard, W. K. Ford, "Rotational Properties of 21 Sc Galaxies with a Large Range of Luminosities and Radii from NGC 4605 (R=4kpc) to UGC 2885 (R=122kpc)", Astrophysical Journal 238:471, 1980.

[8] N. Vittorio and J. Silk, "Fine-scale anisotropy of the cosmic microwave background in a universe dominated by cold dark matter", Astrophysical Journal Part 2 Letters to the Editor 285:L39L43, 1984.

[9] Z. Ahmed, *et al.*, "Results from the Final Exposure of the CDMS II Experiment", arXiv:astro-ph.CO/0912.3592v1, 18 Dec 2009.

[10] R. Bernabei, *et al.*, "First results from DAMA/LIBRA and the combined results with DAMA/NaI", arXiv:astro-ph/0804.2741v1, 17 Apr 2008.

[11] G. Sciolla, "Directional detection of Dark Matter", arXiv:astro-ph/0811.2764v2, 18 Nov 2008.

[12] G. Sciolla, "DM-TPC: a new approach to directional detection of Dark Matter", Princeton High Energy Physics Seminar, January 2008.

[13] A. Green and B. Morgan, "Consequences of statistical sense determination for WIMP directional detection", arXiv:astro-ph/0711.2234v2, 14 Dec 2007.

[14] T. Caldwell, *et al.*, "Transport properties of electrons in CF_4", arXiv:physics.ins-det/0905.2549v1, 15 May 2009.

[15] D. Dujmic *et al.*, "Charge amplification concepts for direction-sensitive dark matter detectors", arXiv:astro-ph/0804.4827v2, 22 Aug 2008.

[16] D. Dujmic *et al.*, "DMTPC-10L: Direction-Sensitive Dark Matter Detector Prototype", arXiv:physics.ins-det/0810.2769v1, 15 Oct 2008.

[17] National Nuclear Data Center, Brookhaven National Laboratory, http://www.nndc.bnl.gov/nudat2/, retrieved 6 March 2010.

[18] National Institute of Standards and Technology, XCOM, http://physics.nist.gov/cgi-bin/Xcom/xcom2, retrieved 21 April 2010.

[19] T. Caldwell, "First Limit from a Surface Run of a 10 Liter Dark Matter Time Projection Chamber", MIT Department of Physics, May 2009.

[20] G. Sciolla, "The DMTPC project", arXiv:astro-ph.IM/0903.3895v1, 23 Mar 2009.

[21] Rest *et al.*, "Residual Images in CCD Detectors", Review of Scientific Instruments 73-2028, 2002.

[22] J. Janesick, "Scientific Charge-Coupled Devices".